Distinguishing trivial and topological quadrupolar insulators by Wannier-Stark ladders

Alexander N. Poddubny*
Ioffe Institute, St. Petersburg 194021, Russia

(Received 15 February 2019; published 13 August 2019)

I study theoretically quadrupolar topological insulators under applied static electric field rotated along the crystal axis. I demonstrate that the energy spectrum of this structure is a Wannier-Stark ladder that naturally visualizes the quantization of nested Wilson loops for the bulk bands. This enables a direct distinction between the topological phase, possessing localized corner states, and the trivial phase, lacking the corner states. The crossover between the topological and trivial cases takes place via the nonadiabatic regime. These results may find applications in the characterization of rapidly emerging higher-order topological phases of light and matter.

DOI: 10.1103/PhysRevB.100.075418

I. INTRODUCTION

Berry phase and Chern numbers are now well-established concepts to characterize the excitations in crystalline solids [1]. Namely, depending on the value of the Chern numbers, calculated for bulk Bloch bands in infinite crystals, the finite samples, made from the same materials, will or will not have topological states propagating along their edges. Various interference techniques have been proposed to measure the Berry phase for Bloch bands, and the correspondence between bulk and edge features has been tested experimentally [2,3].

Recently, a quadrupolar two-dimensional (2D) topological phase has been put forward [4]. Contrary to the traditional 2D topological insulators, the quadrupolar phase has localized fractional quantized corner states, rather than propagating one-dimensional (1D) edge states. Such corner states have been demonstrated experimentally in the microwave [5], electric [6], and optical [7] setups. While corner states are relatively easy to measure in experiment, direct proof of their topological nature is very hard. The topological manifestations of the quadrupole phases are in stark contrast to the traditional topological insulators, being significantly less visual. Namely, instead of the celebrated Berry phase, the bulk topological feature in quadrupolar insulators is the quantized phase of so-called nested Wilson loops [4,8]. The Wilson loops have an inherently non-Abelian nature, which makes them conceptually more difficult to interpret and to measure. The traditional interference techniques developed to probe the Berry phase [2,3,9] are inapplicable. The Wilson loop tomography has so far been developed only for the case of nondegenerate Bloch bands [10], while the quadrupolar phase has doubly degenerate Bloch bands due to the reflection and chiral symmetries [8]. Thus, the fundamental question of measurable bulk manifestations of the quadrupolar topological phase remains open, and a clear protocol to measure the topological invariants in the bulk is highly desired.

Here, I put forward a procedure for bulk spectroscopy of topological features of the quadrupolar phase based on the application of a constant electric field $\boldsymbol{F}$ to the structure. The energy spectrum of a general one-dimensional biased periodic structure is a Wannier-Stark ladder of discrete levels [11–13]. The energy levels E_n of the ladder formed from a given Bloch band depend on the electric field as $E_n = E_n(F = 0) + F(n + c)$, where $n = 0, \pm 1, \ldots$ is the level number [14–16] and c are the Wannier center positions [17]. It is known for a 1D Su-Schrieffer-Heeger (SSH) structure [15] as well as for 2D and three-dimensional topological insulators [14,16,18] that the centers $c = \{dE_n/dF_x\}$ contain information on the topological invariants ($\{x\}$ is the fractional part of x). Here, I extend this concept to the quadrupolar phase in a *rotated* electric field. I demonstrate that the shifts $\{dE/dF_y\}$ are quantized for $F_x \neq 0$, $F_y = 0$ and naturally reveal the topological phases of nested Wilson loops. This provides a transparent connection between the formal mathematical definition of the topological quadrupolar phase and its physical manifestations observable in the bulk.

II. QUADRUPOLAR PHASE IN THE ROTATED ELECTRIC FIELD

The structure under consideration is schematically illustrated in Fig. 1(a) [8]. It can be described by a tight-binding Hamiltonian on a square lattice with alternating intracell and intercell tunneling constants γ and λ (black and red solid lines). Dotted lines correspond to the couplings $-\gamma$ and $-\lambda$. Alternation of the positive and negative couplings ensures the nonzero π flux through the unit cell and opens the band gap in the energy spectrum of the infinite structure [4]. The momentum space Hamiltonian for the periodic structure reads

$$H(k_x, k_y) = \begin{pmatrix} 0 & \gamma + \lambda e^{-ik_x} & 0 & -\gamma - \lambda e^{ik_y} \\ \gamma + \lambda e^{ik_x} & 0 & \gamma + \lambda e^{ik_y} & 0 \\ 0 & \gamma + \lambda e^{-ik_y} & 0 & \gamma + \lambda e^{ik_x} \\ -\gamma - \lambda e^{-ik_y} & 0 & \gamma + \lambda e^{-ik_x} & 0 \end{pmatrix}, \tag{1}$$

where $\boldsymbol{k}$ is the Bloch wave vector and the basis corresponds to the atoms in the unit cell ordered as indicated in Fig. 1(a).

*poddubny@coherent.ioffe.ru

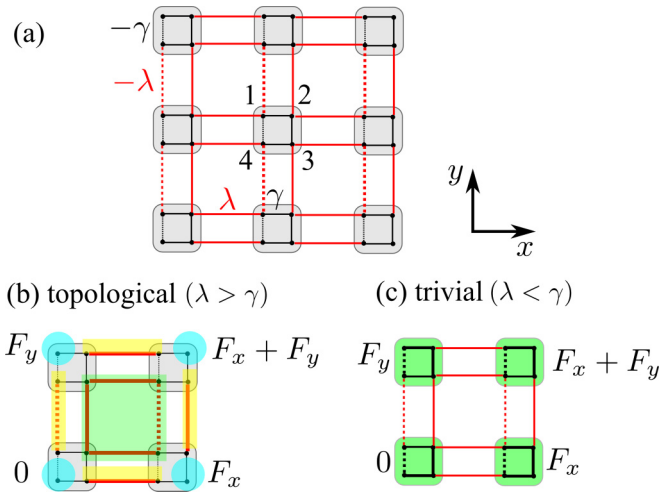

FIG. 1. Scheme of the structure under consideration. (a) Unbiased structure. Biased (b) topological and (c) trivial structures. Green, blue, and yellow shading depicts bulk, corner, and edge states, respectively. External potential in the four unit cells is indicated on the graph.

Depending on the ratio between the couplings γ and λ, the structure can be in either a topological or trivial phase. Namely, for $|\gamma| < |\lambda|$ [Fig. 1(b)] it has corner states (blue circles) and edge states (yellow lines) in addition to the bulk states (green shading). In the opposite case, $|\gamma| > |\lambda|$ [Fig. 1(c)], the corner and edge states are absent. This is seemingly similar to the case of the 1D SSH model, where the termination with a weak tunneling link leads to the formation of a zero-energy edge state [1]. However, the quadrupolar phase is qualitatively different from the 2D SSH lattice because of the presence of negative couplings that are essential for the formation of the bulk band gap and topologically protected corner states, which are absent in a 2D SSH system [7].

The goal of this work is to distinguish between the topological and trivial phases from the bulk, rather than edge, spectral features by applying the external electric field $\boldsymbol{F}$. The main idea is sketched in Figs. 1(b) and 1(c). I assume that all four sites in each unit cell with the discrete coordinates $x, y = 0, \pm1, \pm2, \ldots$ are biased by the same energy $F_x x + F_y y$. In the trivial phase with $\gamma \gg \lambda$ [Fig. 1(c)], each Wannier state is fully located inside the given unit cell. The states have twofold degeneracy, and the energies are $\pm\sqrt{2}\gamma$. The external potential does not split these states and only shifts them independently. In the topological phase with strong intracell couplings, $\lambda \gg \gamma$, the centers of the Wannier functions (green squares) are located between the unit cells [8] [see Fig. 1(b)]. As such, each Wannier state is shared between four unit cells with different values of the external potential, and contrary to the trivial case, the spectrum of the Wannier states will be split by the potential. Next, I prove this crude analysis by the rigorous calculation of the Wannier-Stark ladder.

III. STARK LADDERS FOR $F_y = 0$

I start by considering the structure with the electric field applied along the x direction and the periodic boundary conditions with the wave vector k_y along y. The energy spectra

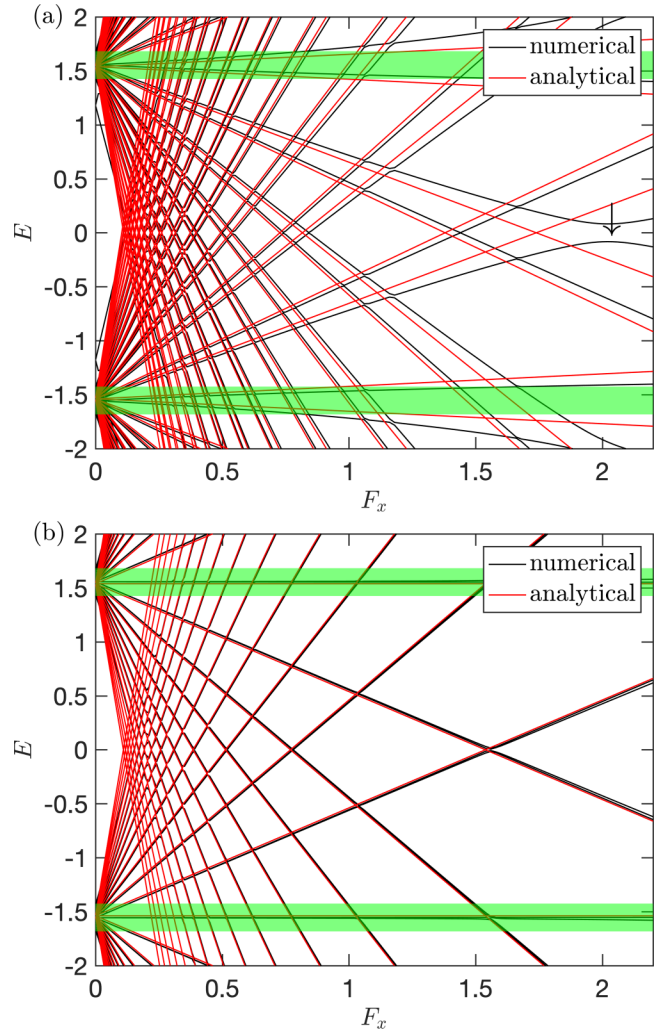

FIG. 2. Stark ladders depending on F_x calculated for $F_y = 0$. (a) and (b) correspond to the topological ($\gamma = 0.2, \lambda = 1$) and trivial ($\gamma = 1, \lambda = 0.2$) structures. Black lines have been calculated numerically, and red lines correspond to the analytical results, Eqs. (2) and (3). Green shading shows the Bloch bands in the unbiased periodic structure. The vertical arrow in (a) indicates the splitting due to the Landau-Zener effect. Periodic boundary conditions with $k_y = 0.5$ have been used along the y direction; open boundary conditions with $N = 10$ unit cells have been used along x.

in the topological and trivial phases are shown in Figs. 2(a) and 2(b), respectively. The calculation demonstrates that the bulk Bloch bands are split due to the electric field and the two fans of levels, with the energies linear in the electric field, emerge from each band. In the limit of $\gamma \ll \lambda$ ($\lambda \ll \gamma$) the energy levels are approximately given by the analytical expressions

$$E^{(\mathrm{topo})}_{n\sigma\pm} \approx \sigma\left(\sqrt{2}\lambda + \frac{\gamma\cos k_y}{\sqrt{2}}\right) + F_x\left(n + \frac{1}{2} \pm \frac{\sqrt{2}}{4}q\right), \quad (2)$$

$$E^{(\mathrm{triv})}_{n\sigma\pm} \approx \sigma\left(\sqrt{2}\gamma + \frac{\lambda\cos k_y}{\sqrt{2}}\right) + nF_x, \quad (3)$$

where $n = 0, \pm1, \ldots$, $\sigma = \pm1$ distinguishes the upper and lower bands, and $q = 1 + \gamma\cos k_y/(2\lambda)$. These equations can

be rigorously obtained as

$$E_{n\sigma\pm} = \int_0^{2\pi} \frac{dk_x}{2\pi} E_\sigma(k_x) + F_x(n + c_\pm), \tag{4}$$

where $c_\pm = \ln(\lambda_\pm)/2\pi i$ and λ are the eigenvalues of the 2×2 Wilson loop operator $W = \exp[-\int_0^{2\pi} dk_x u_\sigma^\dagger \partial u_\sigma/\partial k_x]$. Here, $E_\sigma = \sigma\sqrt{2}\sqrt{\lambda^2 + \gamma^2 + \lambda\gamma(\cos k_x + \cos k_y)}$ are the Bloch band energies, and the 4×2 matrix $u_\sigma = [u_{1\sigma}, u_{2\sigma}]$ contains two Bloch functions, u_1 and u_2, for the corresponding band σ. The detailed derivation is presented in Appendix A. The results are valid in the adiabatic regime, i.e., when the upper and lower Bloch bands can be considered separately and the transitions between them can be ignored.

The analytical answers (2) and (3), calculated from the Wilson loops, are shown by the red lines in Fig. 2 and well describe the direct numerical calculation of the Stark ladder (black lines). This proves that the Stark ladder can be used to calculate the Wannier eigenstates of the Wilson loops. The difference between the topological and trivial cases is now clearly seen. In agreement with the naive explanation in Figs. 1(b) and 1(c), in the topological case the levels (2) are split by $\approx\sqrt{2}F_x/2$, while in the trivial case the states (3) remain almost doubly degenerate.

IV. LANDAU-ZENER EFFECT

Equations (2) and (3) describe two independent Stark ladders formed from the two Bloch bands. However, it can be seen from Fig. 2(a) that, in fact, these ladders are not independent and feature avoided crossings. The largest avoided crossing in Fig. 2(a) takes place at $F_x \approx 2$ and is indicated by an arrow. In Fig. 3 I plot the same levels zoomed in around the field $F_x \approx 2$. The physical origin of the avoided crossing can be understood by noticing that in the limit $\gamma \to 0$ the structure

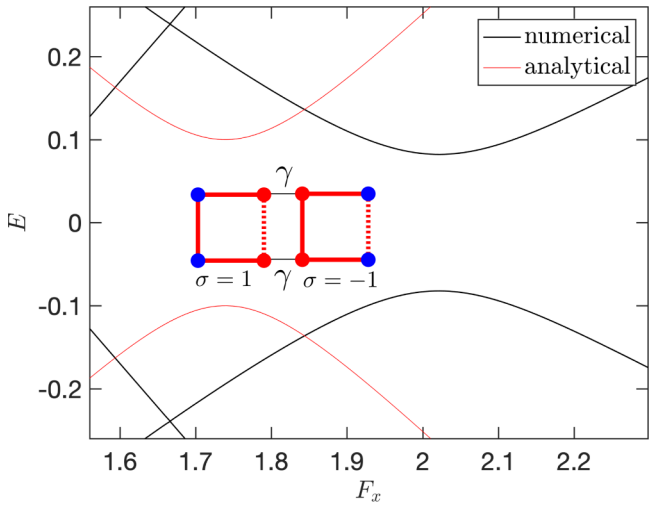

FIG. 3. Spectrum of the Wannier-Stark ladder from Fig. 2(a) enlarged in the vicinity of $F_x = 2$. Black lines show the results of numerical calculation; red lines show the analytical result, Eq. (8). The inset schematically illustrates the spatial structure of the two Wannier functions of the coupled states, with red (blue) circles corresponding to the amplitude of the Wannier function $\psi(x, y) = \pm 1$ (2).

is decoupled into noninteracting 4×4 unit cells with the sites coupled by the links $\pm\lambda$. The tight-binding Hamiltonian for each such cell is

$$\widetilde{H} = \begin{pmatrix} Fx & \lambda & 0 & \lambda \\ \lambda & Fx & -\lambda & 0 \\ 0 & -\lambda & F(x+1) & \lambda \\ \lambda & 0 & \lambda & F(x+1) \end{pmatrix}. \tag{5}$$

Its eigenenergies are equal to

$$E_{x\sigma\pm} = F\left(x - \frac{1}{2}\right) + \sigma\frac{\sqrt{F^2 \pm 4F\lambda\sigma + 8\lambda^2}}{2}, \quad \sigma = \pm 1. \tag{6}$$

In the limit of $\lambda \gg \gamma$ the Wannier functions are fully localized on four sites between the unit cells [see Fig. 1(b)] with the absolute values of all four nonzero wave function components equal to $1/2$. Clearly, for $F = 2\lambda$ one has

$$E_{x,+-} = E_{x+1,-+}, \tag{7}$$

which means that the Wannier functions corresponding to the two adjacent unit cells become degenerate. The parameter n in Eq. (2) specifies the horizontal coordinate; that is, the state n is located between the nth and $(n + 1)$th unit cells. Hence, for $F_x \approx 1.7\lambda$ one has $E_{1,-+} \approx E_{0,+-}$, which means that the Wannier states of upper and lower bands, shifted by one site, become degenerate (see the inset of Fig. 3). The tunneling between these states lifts the degeneracy and opens the gap with the width γ; that is, the energy spectrum in the vicinity of the gap reads

$$\epsilon_\pm = \pm\frac{1}{2}\sqrt{(E_{1,-+} - E_{0,+-})^2 + \gamma^2}. \tag{8}$$

Indeed, the analytical result (8), shown by the red lines in Fig. 3, well describes the exact numerical answer. The only difference is the small horizontal shift of the position of the avoided crossing, which is a next-order effect in the parameter F/λ, not taken into account in the approximation equations (2) and (8). However, the width of the gap for the black curves in Fig. 3 is close to $\gamma = 0.2$, in agreement with Eq. (8). Avoided crossings due to the Landau-Zener effect take place in both topological and trivial cases. However, in the trivial case they start to be discernible for larger electric fields, $F_x \sim 3$ [see Fig. 8(b) in Appendix A], that are beyond the range considered in Fig. 2. The avoided crossings represent the onset of the breakdown of adiabatic approximation when the individual Bloch bands can still be considered separately. At even larger electric fields, $F_x \sim 5$, the electrostatic potential fully overcomes the crystalline potential, the topological features of individual Bloch bands are completely washed out, and the slope $\{\partial E/\partial F_x\}$ is equal to zero in both topological and trivial structures.

V. NESTED WILSON LOOPS VIA THE STARK LADDERS

Figure 2 demonstrates that the application of the electric field modifies the structure in such a way that its eigenstates become the Wannier functions, depending on the wave vector k_y. The phase of the nested Wilson loops proposed in Refs. [4,8] is just the winding number of these functions calculated when k_y is varied across the Brillouin zone. I

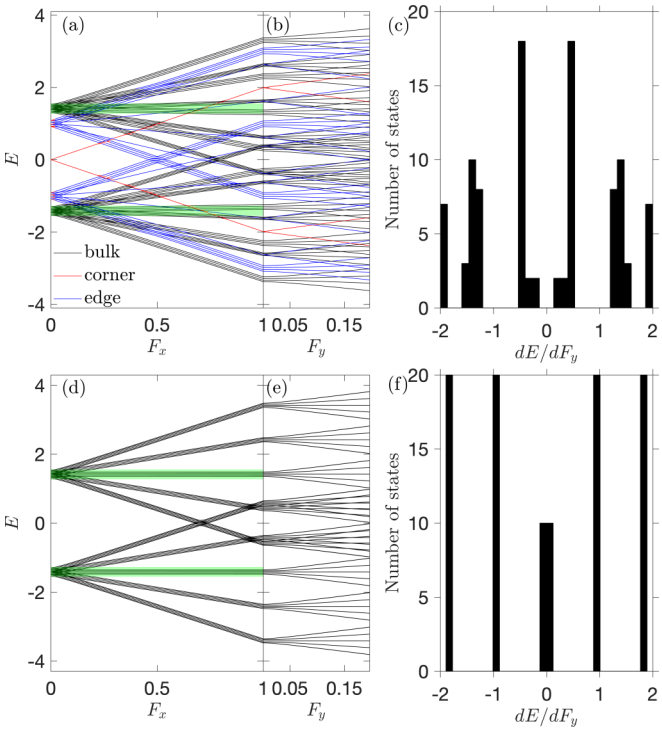

FIG. 4. Stark ladders for an open lattice with 5×5 unit cells depending on (a) and (d) F_x and (b) and (e) F_y in the (a)–(c) topological and (d)–(f) trivial phases with $\gamma = 0.15, \lambda = 1$ and $\gamma = 1, \lambda = 0.15$, respectively. (c) and (f) show the distributions of dE/dF_y for $F_x = 1$, $F_y = 0.1$. Green shading indicates the Bloch bands in the unbiased periodic structure.

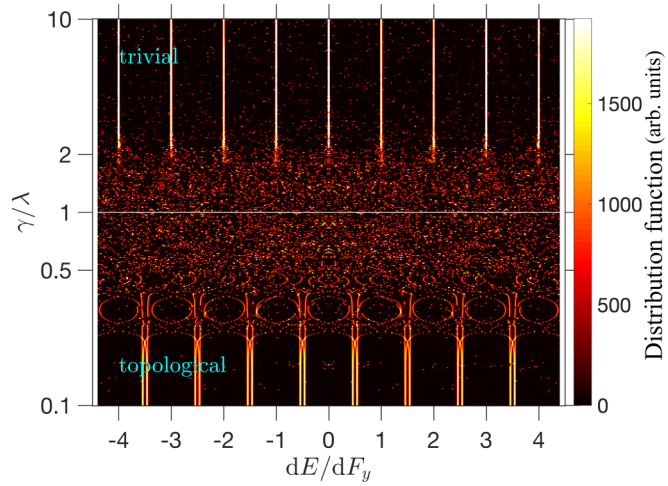

FIG. 5. Color map of the distribution function of the values dE/dF_y for different eigenstates depending on γ for $\lambda = 1$, $F_x = 1$, $F_y = 0.1$. The calculation was performed for the structure with 33×33 unit cells.

have verified numerically that this phase is equal to π (2π) for the topological (trivial) states in Fig. 2(a) [Fig. 2(b)], as expected (see Appendix B). Instead of the calculation of this phase under the periodic boundary conditions along the y direction I will now consider a more realistic situation of a finite structure, open from all four sides. Application of an additional electric field along the y direction, corresponding to the rotation of the total electric field, will then further split the states in Fig. 2. Next, I will demonstrate by an explicit numerical calculation that the resulting *nested Stark ladder* is quantized and directly reflects the phases of the nested Wilson loops.

The results of the calculation are presented in Fig. 4. First, I apply the electric field along the x direction, which leads to the splitting of the Bloch bands for both topological [Fig. 4(a)] and trivial [Fig. 4(d)] structures, similar to Fig. 2. Since now the topological structure is open in both directions, it also has edge and corner modes, indicated by blue and red, respectively, in addition to the bulk modes. The edge (corner) states have been formally defined as the states where the probability of localization at the edge (corner) sites is larger than 0.2. Application of an additional electric field along the y direction splits the spectrum further [Figs. 4(b) and 4(e)]. The key difference between the topological and trivial cases is the distribution of the derivatives dE/dF_y for given $F_x \neq 0$, shown in Figs. 4(d) and 4(f). In the topological structure this distribution has maxima around the *half-integer* values $\pm 1/2, \pm 3/2, \ldots$, i.e., $\{dE/dF_y\} = 1/2$. In order to illustrate this result analytically, I explicitly calculate the Wannier-Stark centers for $F_x \neq 0$, $F_y \neq 0$ in the limit when $\lambda \gg \gamma$. The corresponding tight-binding Hamiltonian is given by

$$\widetilde{H} = F_x x + F_y y + \begin{pmatrix} 0 & \lambda & 0 & \lambda \\ \lambda & F_y & -\lambda & 0 \\ 0 & -\lambda & F_x + F_y & \lambda \\ \lambda & 0 & \lambda & F_x \end{pmatrix}. \tag{9}$$

Its eigenvalues in the lowest order in F are readily found as

$$E_{\sigma\pm} = \sqrt{2}\sigma\lambda + F_x(x + 1/2) + F_y(y + 1/2) \pm \frac{\sqrt{2}}{4}\sqrt{F_x^2 + F_y^2}, \tag{10}$$

where $\sigma = \pm 1$ labels the Bloch band. In the exact limit $F_y = 0$ this result is equivalent to Eqs. (2) and (3). Importantly, Eq. (10) is a clearly nonanalytical function of electric field. The second derivative of the energy over the electric field is well defined and quantized only when either F_x or F_y is nonzero, i.e.,

$$\left\{\frac{\partial E_{\sigma\pm}}{\partial F_y}\right\}\Big|_{F_x \neq 0} = \left\{\frac{\partial E_{\sigma\pm}}{\partial F_x}\right\}\Big|_{F_y \neq 0} = \frac{1}{2}. \tag{11}$$

In the trivial structure the distribution peaks are at the *integer* values $0, \pm 1, \pm 2, \ldots$, i.e., $\{dE/dF_y\} = 0$. The broadening of the peaks in Fig. 4, most distinct in the topological phase, is due to the finite-size effects. This distinction between half-integer and integer values of the derivatives exactly corresponds to the difference between the π and 2π phases of the nested Wilson loops calculated in Ref. [4] for the topological and trivial structures. The advantage of the proposed scheme is that the topological phase arises naturally and can be accessible in finite open systems.

Finally, in Fig. 5 I calculate the variation of the distribution dE/dF_y for given fixed values of F_x and F_y depending on the ratio γ/λ. Due to the larger size of the structure, more peaks are resolved compared to Fig. 4. In order to simplify the presentation, the peak distribution has been convoluted with

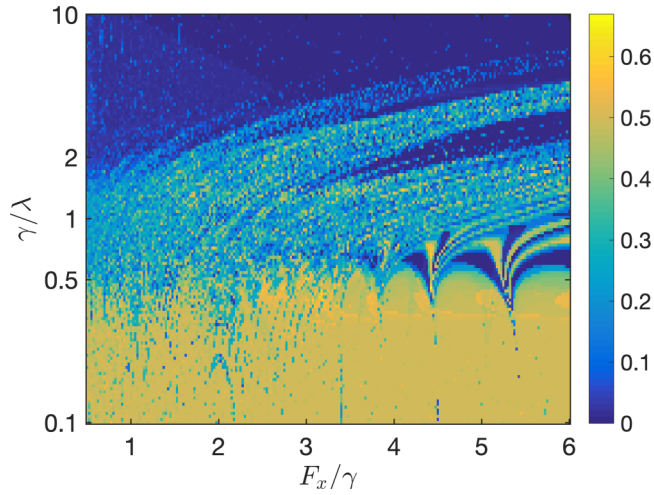

FIG. 6. Color map of the distribution dE/dF_y for the middle level of the Stark ladder depending on γ/λ and the electric field F_x. The calculation was performed for the structure with 17×17 unit cells and $F_y = 0.1$.

a Gaussian function with a dispersion of 0.02. In agreement with Fig. 4, the positions of the peaks shift from half-integer to integer values with the increase of γ. This reflects the transition from the topological to the trivial regime. Notably, the quantization should be quite strong in the experimentally realized regime $\gamma/\lambda \sim 0.17$ [7]. On the other hand, the quantization is not evident in the crossover range with $\gamma \sim \lambda$. A possible explanation is that the energy gap between the Bloch bands becomes narrow for $\gamma \approx \lambda$ and the adiabatic approximation, underlying the construction of the topological indices, is no longer valid. This regime features a rich energy spectrum, strongly sensitive to the electric field and the size of the sample. The calculated dependence of $\{\partial E/\partial F_y\}$ on the electric field and γ/λ is shown in Fig. 6. After the distribution of $\partial E/\partial F_y$ was calculated for a given electric field and a given ratio of γ/λ, I averaged all the values of $\partial E/\partial F_y$ belonging to the range -0.25 to 0.75. Thus, the topological structure with $\gamma \ll \lambda$ should correspond to the mean value of $\{\partial E/\partial F_y\} = 1/2$, and the trivial structure corresponds to $\{\partial E/\partial F_y\} = 0$. These expectations are in general agreement with the numerical results in Fig. 6. However, no distinct quantization is observed for $0.5 < \gamma/\lambda < 1$. Moreover, interesting fine structures appear in the map, for instance, in the region $0.5 < \gamma/\lambda < 1$ at large electric fields $F_x \approx 4.5$, $F_x \approx 5.5$. The fine structure strongly depends on the specific value of $F_y \ll 1$ for which the distribution $\{\partial E/\partial F_y\}$ is calculated and also on the size of the structure. The explanation can be related to the nonadiabaticity or even to the fractal spectrum of the Stark ladder, which might emerge at the irrational directions of the electric field [19–21].

The behavior of the Stark shifts for an arbitrary field direction is also quite instructive. In the topological structure with $\gamma \ll \lambda$, the Stark shifts are $E(\boldsymbol{F}) - E(0) = (F_x + F_y)/2 \pm \sqrt{2}|\boldsymbol{F}|/4$. While this is clearly a nonanalytical function of the electric field $\boldsymbol{F}$, the derivatives $\{dE/dF_y\}$ and $\{dE/dF_x\}$ are quantized when the field is applied along the x and y directions, respectively. So far, I have focused on the Stark ladder quantization for the electric field oriented close to the crystalline axis. In the considered case of the adiabatic regime and the relatively small finite structures, the distinction between rational and irrational directions should be less important, so it is out of the scope of the present study.

VI. SUMMARY

To summarize, I have introduced the concept of bulk spectroscopy of topological invariants in the quadrupolar insulators by relating the quantized phases of nested Wilson loops to the spectra of Wannier-Stark ladders. Experimental implementation requires a comparison of the energy spectra for different external potentials. In optics, this could be achieved for a two-dimensional array of ring resonators with thermally tunable on-site energies, similar to the experiment in Ref. [3]. The energy spectra can be extracted from the measured transmission maps by using the tomography procedure proposed in Ref. [22]. Instead of a single tunable sample, one could also fabricate a set of rigid samples with different effective electric fields, as was already done for the characterization of topological photonic quasicrystals [23]. An even simpler experimental realization is possible for the topoelectric circuits [6], where the on-site energies of individual sites can be tuned by introducing nonlinear elements [24] and the local on-site voltages can be probed directly. The proposed scheme could also be generalized to other higher-order topological insulators [25].

ACKNOWLEDGMENTS

I acknowledge the financial support from the Foundation for Advancement of Theoretical Physics and Mathematics "Basis" and the Russian Foundation for Basic Research Grants No. 18-29-20037 and 18-32-20065.

APPENDIX A: STARK LADDERS FOR $F_y = 0$

Here, I will reiterate the general procedure to calculate the spectrum of a periodic structure in a constant electric field [10,15] for the case of a quadrupolar insulator. I assume that the electric field is applied only along the x direction and periodic boundary conditions with the wave vector k_y are applied along the y direction. The energy spectrum can be then calculated from the following system of equations:

$$\begin{aligned}(H_0 + F_x x)u_x + H_+ u_{x+1} + H_- u_{x-1} &= E u_x, \quad 1 < x < N,\\ (H_0 + F)u_1 + H_+ u_2 &= E u_1,\\ (H_0 + FN)u_N + H_- u_{N-1} &= E u_N,\end{aligned} \tag{A1}$$

where

$$H_0 = \begin{pmatrix} 0 & \gamma & 0 & -\gamma - \lambda e^{ik_y} \\ \gamma & 0 & \gamma + \lambda e^{ik_y} & 0 \\ 0 & \gamma + \lambda e^{-ik_y} & 0 & \gamma \\ -\gamma - \lambda e^{-ik_y} & 0 & \gamma & 0 \end{pmatrix},$$

$$H_+ = \lambda \begin{pmatrix} 0 & 0 & 0 & 0 \\ 1 & 0 & 0 & 0 \\ 0 & 0 & 0 & 1 \\ 0 & 0 & 0 & 0 \end{pmatrix}, \quad H_- = H_+^\dagger. \tag{A2}$$

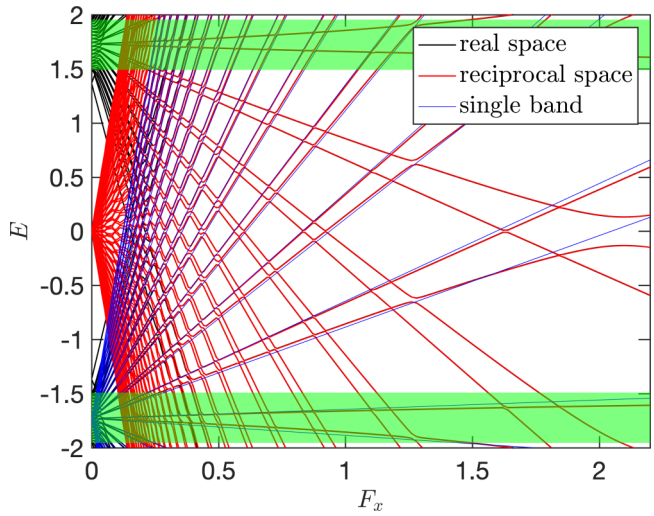

FIG. 7. Stark ladders depending on F_x calculated for $F_y = 0$. Black lines correspond to results obtained from Eq. (A1) in the real space, red lines were calculated from Eq. (A9) in the reciprocal space, and blue lines were found from Eq. (A12) in the single-band approximation. The calculation was performed for $\gamma = 0.4$, $\lambda = 1$, $k_y = 0.5$, $N = 10$.

Here, N is the number of unit cells in the x direction taken into account. This is the approach used to calculate the black curves in Fig. 2 in the main text. Alternatively, one can consider an infinite structure and look for the solution in the form

$$\psi(x) = \int_0^{2\pi} \frac{dk_x}{2\pi} u(k_x) e^{ik_x x}, \tag{A3}$$

with $u(k_x)$ satisfying the periodic gauge

$$u(k_x + 2\pi) = u(k_x). \tag{A4}$$

Substituting Eq. (A3) into Eq. (A1), I obtain

$$iF \frac{\partial}{\partial k_x} u(k_x) + H(k_x, k_y) u(k_x) = E u(k_x), \tag{A5}$$

where the Hamiltonian

$$H(k_x, k_y) = \begin{pmatrix} 0 & \gamma + \lambda e^{-ik_x} & 0 & -\gamma - \lambda e^{ik_y} \\ \gamma + \lambda e^{ik_x} & 0 & \gamma + \lambda e^{ik_y} & 0 \\ 0 & \gamma + \lambda e^{-ik_y} & 0 & \gamma + \lambda e^{ik_x} \\ -\gamma - \lambda e^{-ik_y} & 0 & \gamma + \lambda e^{-ik_x} & 0 \end{pmatrix} \tag{A6}$$

is the same as in Eq. (1) of the main text. The solution of Eq. (A5) can then be sought in the form

$$u(k_x) = e^{-i\frac{Ek_x}{F_x}} V(k_x) u(0), \tag{A7}$$

$$V(k_x) = \exp\left(\frac{i}{F_x} \int_0^{k_x} dk_x' H(k_x') \right). \tag{A8}$$

Substituting Eq. (A8) into Eq. (A4), we find that $u(0)$ should be the eigenvector of $V(2\pi)$ with the eigenvalue 1 and

$$E = F_x(n + c_\nu), \quad c_\nu = \frac{1}{2\pi i} \ln \tilde{\lambda}_\nu, \quad \nu = 1, \ldots, 4, \tag{A9}$$

where $\tilde{\lambda}_\nu$ are the eigenvalues of the 4×4 matrix $V(2\pi)$.

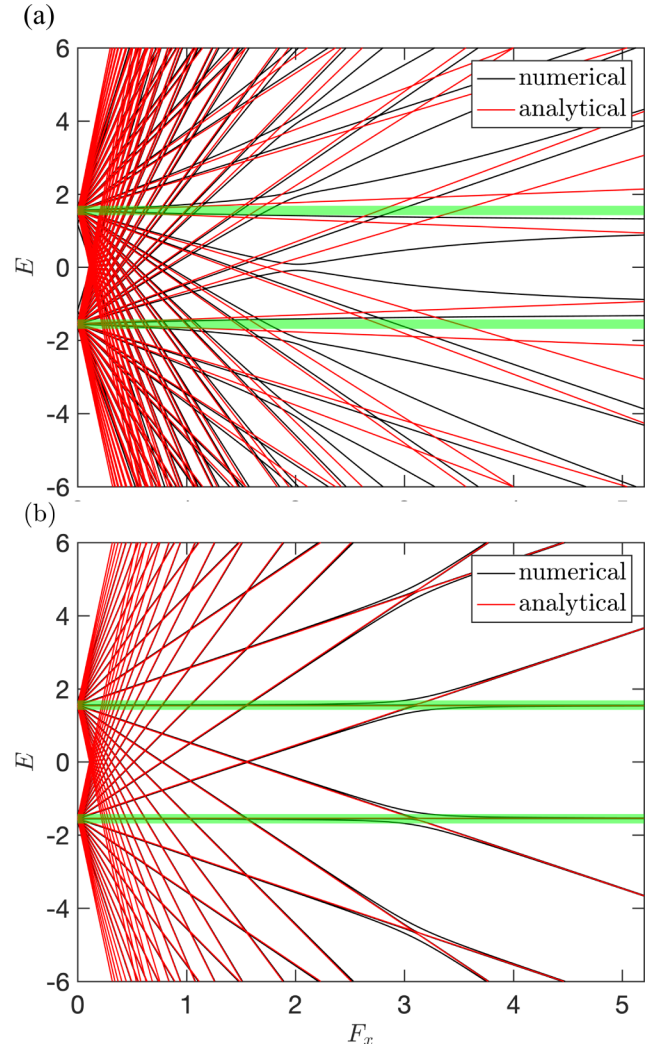

FIG. 8. Stark ladders depending on F_x calculated for $F_y = 0$. (a) and (b) correspond to the topological ($\gamma = 0.2$, $\lambda = 1$) and trivial ($\gamma = 1$, $\lambda = 0.2$) structures. Black lines were calculated numerically, and red lines correspond to the analytical results from Eqs. (A12) and Eq. (A13). Green shading shows the Bloch bands in the unbiased periodic structure. Periodic boundary conditions with $k_y = 0.5$ have been used along the y direction; open boundary conditions with $N = 10$ unit cells have been used along x.

Equation (A9) is equivalent to Eqs. (A1) in the limit $N \to \infty$, as can be seen by comparing the black and red lines in Fig. 7. The discrepancy at small electric fields is due to the finite value of N used to solve Eqs. (A1) and the finite number of $n = -14, \ldots, 14$ used for plotting Eq. (A9).

One can simplify Eq. (A9) by ignoring the interaction between the Stark ladders originating from the upper and lower Bloch bands (i.e., the Landau-Zener effect). Specifically, I will consider the lower Bloch band with the energy

$$E_- = -E_+ = -\sqrt{2}\sqrt{\lambda^2 + \gamma^2 + \lambda\gamma(\cos k_x + \cos k_y)}. \tag{A10}$$

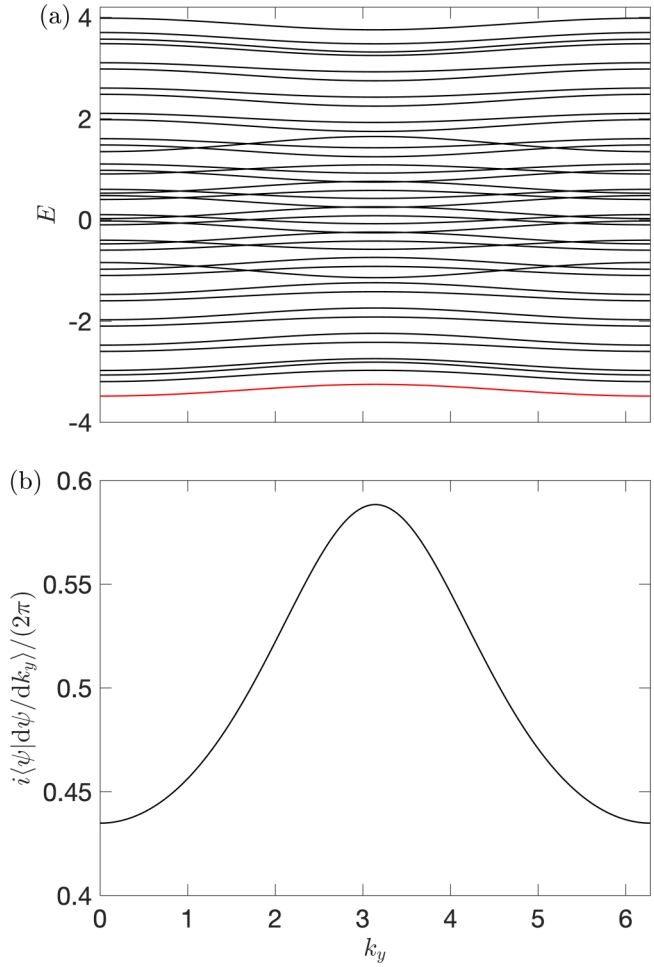

FIG. 9. (a) Dependence of the Wannier-Stark ladder spectrum on k_y. (b) Integrand of the Zak phase for the lowest-energy state, shown in red in (a). $\gamma = 0.15$, $\lambda = 1$, $N = 5$, $F = 0.5$.

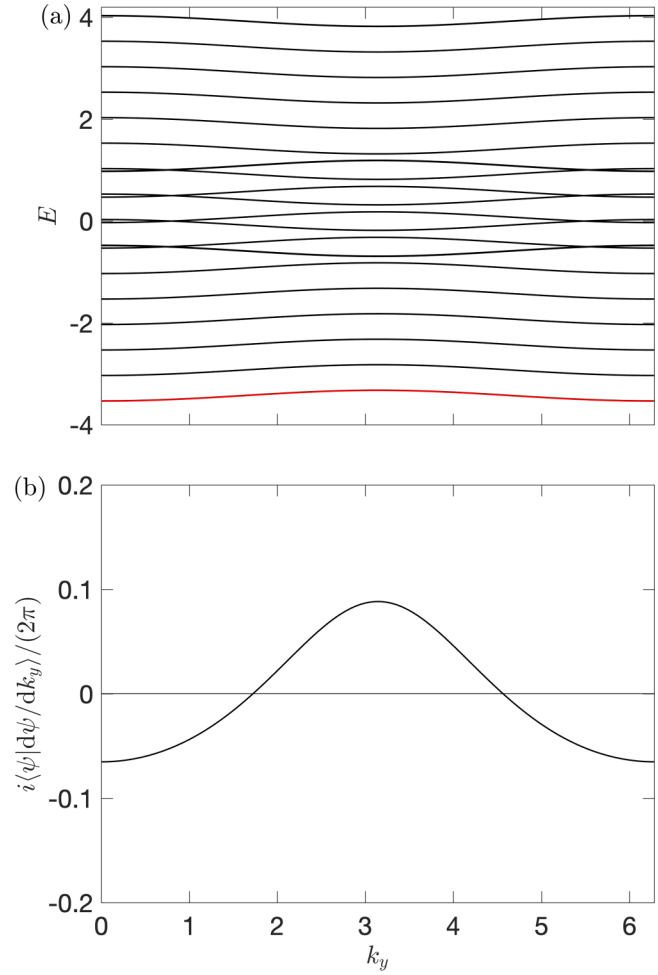

FIG. 10. Same as Fig. 9, but for the trivial phase $\gamma = 1$, $\lambda = 0.15$.

The two eigenvectors $u_{1,2-}$ of the Hamiltonian (1) corresponding to the bottom Bloch band are

$$[u_{1-}, u_{2-}] \equiv u_- = \frac{1}{\sqrt{2}} \begin{pmatrix} 1 & 0 \\ -\frac{\gamma+\lambda e^{ik_x}}{E_+} & -e^{ik_x}\frac{\gamma+\lambda e^{ik_y}}{E_+} \\ 0 & e^{ik_x} \\ \frac{\gamma+\lambda e^{-ik_y}}{E_+} & -e^{ik_x}\frac{\gamma+\lambda e^{-ik_x}}{E_+} \end{pmatrix}. \quad \text{(A11)}$$

Next, we project Eq. (A5) into the subspace spanned by the functions u_{1-} and u_{2-}. Namely, we substitute $u(k)$ in the form $A_1 u_{1-} + A_2 u_{2-}$ into Eq. (A5) and solve for $A_{1,2}(k_x)$ satisfying Eq. (A4). This results in the energy spectrum

$$E = \int_0^{2\pi} \frac{ek_x}{2\pi} E(k_x) + F_x(n + c_\nu), \quad c_\nu = \frac{\ln \lambda_\nu}{2\pi i}, \quad \nu = 1, 2, \quad \text{(A12)}$$

with λ_ν being the eigenvalues of the 2×2 Wilson loop

$$W = \exp\left[-\int_0^{2\pi} \frac{dk_x}{2\pi} u_-^\dagger \frac{\partial u_-}{\partial k_x}\right]. \quad \text{(A13)}$$

This is Eq. (4) from the main text. Blue lines in Fig. 7, calculated according to Eq. (A12), well describe the results of exact calculation with the only difference being the avoided crossings between the Stark ladders originating from the upper and lower allowed bands (i.e., the Landau-Zener effect). These avoided crossings stem from the coupling between the two bands induced by the electric field and hence are not captured by the single-band approximation. In the case when $\gamma \ll \lambda$ ($\lambda \ll \gamma$), the u_- matrix is simplified, and the integral over k_x in Eq. (A13) can be calculated analytically. This results in Eqs. (2) and (3).

Figure 8 shows the Stark ladder in the topological [Fig. 8(a)] and trivial [Fig. 8(b)] cases in the wider range of electric fields up to $F_x = 5.5$. It demonstrates that while for low electric fields the numerical results well agree with the single-band adiabatic approximation (A12), for large electric fields the adiabatic approximation breaks down. First, the avoided crossings appear between the levels corresponding to different bands, starting from $F_x \sim 2$ in the topological and $F_x \sim 3$ in the trivial case. Second, the slope of the dependence $\{\partial E/\partial F_x\}$ changes at large fields for the topological structure and becomes equal to zero, similar to the case of trivial structure [see Fig. 8(a)]. This is similar to the behavior of the one-dimensional Su-Schrieffer-Heeger model [15]: a large external electrostatic potential completely overcomes the crystalline potential, and the topological features of individual Bloch bands are washed out. The avoided crossings between

the individual levels present the onset of this breakdown. They result from the Landau-Zener effect and are analyzed in more detail in Sec. IV.

APPENDIX B: ZAK PHASE FOR THE WANNIER STATES

In this Appendix I present an explicit calculation of the Zak phase for the eigenstates of the Wannier-Stark ladder found from Eqs. (A1). To this end I fix the value of F_x and calculate the dependence of the eigenstate on k_y varying from 0 to 2π. In order to fix the gauge I set the component of the $4N$-length eigenvector of Eq. (A1) with the largest absolute value to be real. The Zak phase is defined as [1]

$$\varphi = i\int_0^{2\pi} dk_y \langle\psi|\partial_{k_y}|\psi\rangle. \tag{B1}$$

The calculation in Fig. 9 clearly demonstrates that the Zak phase for the lowest eigenstate is equal to π, which means that the structure is in the nontrivial phase, in full agreement with Ref. [8]. I have numerically verified that the same holds for all the eigenstates. On the other hand, in the trivial phase the Zak phase cancels out [see Fig. 10(b)]. This presents an explicit confirmation that the eigenstates of the Wannier-Stark ladder in the electric field applied along the x direction inherit the topological features of the structure.

The crossings between different levels in Fig. 10 are accidental rather than appearing from the general symmetry arguments. As such, they do not affect the overall quantization of the Zak phase: the crossing points can just be excluded from the integrals. In the actual calculation of the Stark ladder the topological indices are evaluated in the real space by analyzing the dependence on the electric field F_y, and this accidental degeneracy does not play a role. The only requirement is the small step in the electric field δF_y when evaluating numerically the derivative $\partial E/\partial F_y = [E(F_y + \delta F_y) - E(F_y)]/\delta F_y$, so that the order of the levels remains the same.

[1] B. Bernevig and T. Hughes, *Topological Insulators and Topological Superconductors* (Princeton University Press, Princeton, NJ, 2013).

[2] M. Atala, M. Aidelsburger, J. T. Barreiro, D. Abanin, T. Kitagawa, E. Demler, and I. Bloch, Direct measurement of the Zak phase in topological Bloch bands, Nat. Phys. **9**, 795 (2013).

[3] S. Mittal, S. Ganeshan, J. Fan, A. Vaezi, and M. Hafezi, Measurement of topological invariants in a 2D photonic system, Nat. Photonics **10**, 180 (2016).

[4] W. A. Benalcazar, B. A. Bernevig, and T. L. Hughes, Quantized electric multipole insulators, Science **357**, 61 (2017).

[5] C. W. Peterson, W. A. Benalcazar, T. L. Hughes, and G. Bahl, A quantized microwave quadrupole insulator with topologically protected corner states, Nature (London) **555**, 346 (2018).

[6] S. Imhof, C. Berger, F. Bayer, J. Brehm, L. W. Molenkamp, T. Kiessling, F. Schindler, C. H. Lee, M. Greiter, T. Neupert, and R. Thomale, Topolectrical-circuit realization of topological corner modes, Nat. Phys. **14**, 925 (2018).

[7] S. Mittal, V. Vikram Orre, G. Zhu, M. A. Gorlach, A. Poddubny, and M. Hafezi, Photonic quadrupole topological phases, Nat. Photonics (2019), doi:10.1038/s41566-019-0452-0.

[8] W. A. Benalcazar, B. A. Bernevig, and T. L. Hughes, Electric multipole moments, topological multipole moment pumping, and chiral hinge states in crystalline insulators, Phys. Rev. B **96**, 245115 (2017).

[9] A. V. Poshakinskiy, A. N. Poddubny, and M. Hafezi, Phase spectroscopy of topological invariants in photonic crystals, Phys. Rev. A **91**, 043830 (2015).

[10] T. Li, L. Duca, M. Reitter, F. Grusdt, E. Demler, M. Endres, M. Schleier-Smith, I. Bloch, and U. Schneider, Bloch state tomography using Wilson lines, Science **352**, 1094 (2016).

[11] E. E. Mendez and G. Bastard, Wannier-Stark ladders and Bloch oscillations in superlattices, Phys. Today **46**(6), 34 (1993).

[12] S. Shevchenko, S. Ashhab, and F. Nori, Landau–Zener–Stückelberg interferometry, Phys. Rep. **492**, 1 (2010).

[13] M. Glück, A. R. Kolovsky, and H. J. Korsch, Wannier-Stark resonances in optical and semiconductor superlattices, Phys. Rep. **366**, 103 (2002).

[14] M. Taherinejad, K. F. Garrity, and D. Vanderbilt, Wannier center sheets in topological insulators, Phys. Rev. B **89**, 115102 (2014).

[15] D. N. Maksimov, E. N. Bulgakov, and A. R. Kolovsky, Wannier-Stark states in double-periodic lattices. I. One-dimensional lattices, Phys. Rev. A **91**, 053631 (2015).

[16] W.-R. Lee and K. Park, Direct manifestation of topological order in the winding number of the Wannier-Stark ladder, Phys. Rev. B **92**, 195144 (2015).

[17] N. Marzari and D. Vanderbilt, Maximally localized generalized Wannier functions for composite energy bands, Phys. Rev. B **56**, 12847 (1997).

[18] A. R. Kolovsky, Topological phase transitions in tilted optical lattices, Phys. Rev. A **98**, 013603 (2018).

[19] I. A. Dmitriev and R. A. Suris, Damping of Bloch oscillations in quantum dot superlattices: A general approach, Semiconductors **36**, 1364 (2002).

[20] A. R. Kolovsky and H. J. Korsch, Bloch oscillations of cold atoms in two-dimensional optical lattices, Phys. Rev. A **67**, 063601 (2003).

[21] C. R. Dean, L. Wang, P. Maher, C. Forsythe, F. Ghahari, Y. Gao, J. Katoch, M. Ishigami, P. Moon, M. Koshino, T. Taniguchi, K. Watanabe, K. L. Shepard, J. Hone, and P. Kim, Hofstadter's butterfly and the fractal quantum Hall effect in moiré superlattices, Nature (London) **497**, 598 (2013).

[22] M. A. Gorlach, M. Di Liberto, A. Recati, I. Carusotto, A. N. Poddubny, and C. Menotti, Simulation of two-boson bound states using arrays of driven-dissipative coupled linear optical resonators, Phys. Rev. A **98**, 063625 (2018).

[23] F. Baboux, E. Levy, A. Lemaître, C. Gómez, E. Galopin, L. Le Gratiet, I. Sagnes, A. Amo, J. Bloch, and E. Akkermans, Measuring topological invariants from generalized edge states in polaritonic quasicrystals, Phys. Rev. B **95**, 161114(R) (2017).

[24] Y. Hadad, J. C. Soric, A. B. Khanikaev, and A. Alù, Self-induced topological protection in nonlinear circuit arrays, Nat. Electronics **1**, 178 (2018).

[25] F. Schindler, A. M. Cook, M. G. Vergniory, Z. Wang, S. S. P. Parkin, B. A. Bernevig, and T. Neupert, Higher-order topological insulators, Sci. Adv. **4**, eaat0346 (2018).